PHYSICAL REVIEW D **88,** 103009 (2013)

Collapse of nonlinear gravitational waves in moving-puncture coordinates

David Hilditch,[1] Thomas W. Baumgarte,[2,3] Andreas Weyhausen,[1] Tim Dietrich,[1] Bernd Brügmann,[1]
Pedro J. Montero,[2] and Ewald Müller[2]

[1]*Friedrich-Schiller-Universität Jena, 07743 Jena, Germany*
[2]*Max-Planck-Institute für Astrophysik, Karl-Schwarzschild-Strasse 1, D-85748 Garching bei München, Germany*
[3]*Department of Physics and Astronomy, Bowdoin College, Brunswick, Maine 04011, USA*

(Received 20 September 2013; published 22 November 2013)

We study numerical evolutions of nonlinear gravitational waves in moving-puncture coordinates. We adopt two different types of initial data—Brill and Teukolsky waves—and evolve them with two independent codes producing consistent results. We find that Brill data fail to produce long-term evolutions for common choices of coordinates and parameters, unless the initial amplitude is small, while Teukolsky wave initial data lead to stable evolutions, at least for amplitudes sufficiently far from criticality. The critical amplitude separates initial data whose evolutions leave behind flat space from those that lead to a black hole. For the latter we follow the interaction of the wave, the formation of a horizon, and the settling down into a time-independent trumpet geometry. We explore the differences between Brill and Teukolsky data and show that for less common choices of the parameters—in particular negative amplitudes—Brill data can be evolved with moving-puncture coordinates and behave similarly to Teukolsky waves.

DOI: 10.1103/PhysRevD.88.103009 PACS numbers: 95.30.Sf, 04.25.D−

I. INTRODUCTION

The first successful simulations of binary black hole merger and coalescence [1–3] marked a massive breakthrough in the field of numerical relativity. Since then, numerous simulations of black hole binaries have produced important results, including predictions of the emitted gravitational wave forms for various binary configurations. Many of these simulations have been performed with some version of the Baumgarte-Shapiro-Shibata-Nakamura (BSSN) formulation [4–6]. Their success depends crucially on the use of suitable coordinate conditions. For simulations of compact objects, the 1 + log slicing condition [7] together with the Gamma-driver shift condition [8,9] have proven versatile. The combination is often referred to as ''moving-puncture'' coordinates.

The geometric properties of moving-puncture coordinates have been analyzed by [10–14]. These studies showed that dynamical evolutions of a Schwarzschild black hole result in spatial slices that do not encounter the central singularity, and instead asymptote to a finite areal radius. In a Penrose diagram, these slices connect spatial infinity in one universe with timelike infinity in the other. In an embedding diagram (see, e.g., Fig. 2 in [13]) the slices resemble a trumpet, which explains why they are called ''trumpet'' slices.

It is not obvious that, in general, moving-puncture coordinates work well for regular initial data that collapse to a black hole. Following earlier work [15], two independent calculations [16,17] considered stellar collapse and found that, in the cases considered, moving-puncture coordinates can indeed lead to stable evolution, with the newly formed black hole expressed in a trumpet geometry. The primary motivation for this paper is to answer the following question: *in what scenario, if any, can the collapse of gravitational waves to a black hole be followed in moving-puncture coordinates?* To do this we consider axisymmetric vacuum data of two types, namely Brill and Teukolsky waves [18,19].

A secondary motivation comes from the context of critical collapse (see [20,21] for reviews). Critical collapse in gravitational systems was first discovered by Choptuik [22], who considered scalar fields in spherical symmetry. Parametrizing the strength of the initial data with some parameter, say A, it is found that for sufficiently small A the fields ultimately propagate to infinity and leave behind flat space, possibly after interacting in a nonlinear fashion. Above a critical value $A_\star$ of the amplitude, however, the fields collapse and form a black hole. In the vicinity of $A_\star$ the solution displays critical behavior familiar from other fields of physics.

Similar behavior was found in other gravitational systems. Of relevance here, Abrahams and Evans [23,24] reported critical phenomena in the collapse of axisymmetric gravitational waves. Unfortunately it has proven difficult to reproduce these results. Various authors have studied the evolution of gravitational wave initial data (see Table I for a list of published results), but only Sorkin [30] has been able to identify critical behavior. Even his study, which adopted Brill wave initial data [18,31] and used a generalized harmonic code [1,32,33] in axisymmetry [34], required fine-tuning of free parameters in the gauge source functions that specify the coordinates. Sorkin found qualitative differences from the earlier work. For example, he reports that, at least for part of the parameter space, the waves collapse to form a singularity on a ring in the equatorial plane, whereas Abrahams and Evans [24] found the singularity to form at

TABLE I. Summary of published results on numerical simulations of nonlinear waves.

Authors	Year	Data type	Slicing and gauge	References	Comments
Eppley	1978	Brill	Maximal slicing/quasi-isotropic	[25]	Small amplitude waves only
Abrahams & Evans	1992	Teukolsky	Maximal slicing/quasi-isotropic	[23,24]	Reported critical behavior
Alcubierre *et al.*	2000	Brill	Maximal slicing/zero shift	[26]	
Garfinkle & Duncan	2001	Brill	Maximal slicing/quasi-isotropic	[27]	
Santamaria	2006	Brill	Multiple choices	[28]	
Rinne	2008	Brill	Maximal slicing/quasi-isotropic	[29]	
Sorkin	2011	Brill	Family of gauge source functions	[30]	Reported critical behavior

the center. Sorkin also found a significantly larger value for the critical amplitude than in earlier studies of the same data.

Following the first question, our final aim is to report that under evolution Brill data [18,31] behave differently from Teukolsky data [19], at least for common choices of the parameters. These Brill waves fail to produce stable, long-term evolutions when evolved with moving-puncture coordinates, unless the initial amplitude is small, while Teukolsky data lead to stable evolutions, unless the initial amplitude is close to criticality. The obvious question is the following: *why is it so difficult to evolve Brill wave data?* To *begin* to address this question we identify qualitative differences in the two initial data types and examine the effect of these differences on the evolution. We also note that the original studies of Abrahams and Evans [23,24] adopted Teukolsky wave initial data. Since then, all published work that we are aware of has used Brill wave initial data (see Table I)—perhaps because the latter can be constructed more easily. This choice may have contributed to the difficulty of studying critical phenomena in vacuum spacetimes.

The paper is organized as follows. In Sec. II we review relevant results from the 3 + 1 split of spacetime. In Sec. III we discuss the construction and evolution of Brill and Teukolsky wave data. In Sec. IV we discuss some possible causes of the differences in behavior between the two types. In Sec. V we summarize. Appendix contains a description of the codes employed. We adopt geometrized units $G = c = 1$.

II. THE 3 + 1 DECOMPOSITION

Space-time split: We solve Einstein's field equations in vacuum with the help of a 3 + 1 decomposition ([35,36]; see [37–39] for pedagogical introductions). We write the spacetime metric in the form

$$\begin{aligned} ds^2 &= g_{ab}dx^a dx^b \\ &= -\alpha^2 dt^2 + \gamma_{ij}(dx^i + \beta^i dt)(dx^j + \beta^j dt), \end{aligned} \quad (1)$$

where α is the lapse function, β^i the shift vector, and γ_{ij} the spatial metric. Here and in the following indices $a, b, \ldots$ run over spacetime indices, while indices $i, j, \ldots$ run over space indices only. Einstein's field equations split into two sets, namely the Hamiltonian and momentum constraints and the evolution equations.

Constraint and evolution equations: The Hamiltonian and momentum constraints are given by

$$R + K^2 - K_{ij}K^{ij} = 0, \quad (2)$$

$$D_j K^{ij} - D^i K = 0. \quad (3)$$

Here R is the trace of the Ricci tensor R_{ij} associated with the spatial metric γ_{ij}, D_i is the covariant derivative associated with γ_{ij}, K_{ij} is the extrinsic curvature

$$K_{ij} = -\frac{1}{2\alpha}\partial_t \gamma_{ij} + D_{(i}\beta_{j)}, \quad (4)$$

and $K = \gamma^{ij}K_{ij}$ its trace.

Equation (4) can be solved for the time derivative of the spatial metric γ_{ij}, which provides one of the two evolution equations. A second evolution equation results from Einstein's equations and determines the time derivative of the extrinsic curvature. We construct numerical solutions to the constraint and evolution equations, using the two independent codes described in Appendix . We employ a conformal transformation of the spatial metric,

$$\gamma_{ij} = \psi^4 \bar{\gamma}_{ij}, \quad (5)$$

where ψ is a conformal factor and $\bar{\gamma}_{ij}$ a conformally related metric. The Hamiltonian constraint can then be written as an elliptic equation for the conformal factor,

$$\bar{D}^2\psi = \frac{\psi}{8}\bar{R} + \frac{\psi^5}{8}(K^2 - K_{ij}K^{ij}), \quad (6)$$

where $\bar{D}^2$ and $\bar{R}$ are the Laplace operator and Ricci scalar associated with $\bar{\gamma}_{ij}$. Solving the constraints results in data describing the gravitational fields at one instant of time.

Gauge choice: The lapse function α and the shift vector β^i encode the coordinate freedom and can be chosen freely. Most often we use the 1 + log slicing condition [7] and the Gamma-driver shift [8,9] conditions,

$$(\partial_t - \beta^j\partial_j)\alpha = -2\alpha K, \quad (7)$$

$$(\partial_t - \beta^j\partial_j)\beta^i = \mu_S\bar{\Gamma}^i - \eta\beta^i, \quad (8)$$

where $\bar{\Gamma}^i \equiv \bar{\gamma}^{jk}\bar{\Gamma}^i_{jk}$, are called conformal connection functions. Here $\bar{\Gamma}^i_{jk}$ are the connection coefficients associated with the conformally related metric $\bar{\gamma}_{ij}$. At $t = 0$ we initialize the lapse and shift with $\alpha = 1$ and $\beta^i = 0$. Together, the two conditions are usually called "moving-puncture" coordinates. We consider alternatives to (7) and (8); in particular we use a "nonadvective" version of the above conditions, in which the shift terms on the left-hand sides are omitted, and evolutions with zero shift.

III. NUMERICAL EVOLUTIONS OF BRILL AND TEUKOLSKY WAVES

A. Brill waves

Initial data: Brill wave initial data [18,31] can be constructed by writing the spatial metric γ_{ij} in the form

$$dl^2 = \gamma_{ij}dx^i dx^j = \psi^4[e^{2q}(d\rho^2 + dz^2) + \rho^2 d\phi^2]. \quad (9)$$

Here ρ, z, and ϕ are cylindrical coordinates, ψ is the conformal factor, and $q = q(r, \theta)$ is an arbitrary axisymmetric seed function. Under the further assumption of time symmetry the momentum constraint (3) is solved identically, and the Hamiltonian constraint (2) reduces to a linear elliptic equation for ψ,

$$\nabla^2\psi = -\frac{\psi}{4}\left(\frac{\partial^2 q}{\partial\rho^2} + \frac{\partial^2 q}{\partial z^2}\right), \quad (10)$$

where ∇^2 denotes the flat, three-dimensional Laplace operator. For our applications we choose the seed function q according to

$$q(\rho, z) = A\left(\frac{\rho}{\sigma}\right)^2 e^{-[(\rho-\rho_0)^2 - z^2]/\sigma^2}, \quad (11)$$

where A is a measure of the resulting wave amplitude, σ of the wavelength, and ρ_0 of the center of the initial wave. Throughout we set $\sigma = 1$, which determines the units of all dimensional results. Given choices for these parameters we solve Eq. (10) for ψ and insert the result, together with q, into the metric (9). We experiment with different values of A and ρ_0 in what follows. For a given choice of the parameter ρ_0 in the Brill seed function (11), the resulting spacetime depends on the amplitude A, although some gauge conditions may be unsuitable for computing it. In this section we will focus on "central" waves with $\rho_0 = 0$.

Evolution of $A = 1$ centered Brill data: Following previous attempts in other coordinate systems (see Table I) we explore the dynamical evolution of Brill wave initial data with moving-puncture coordinates. For small A, the waves represent a linear perturbation of flat space that will propagate to spatial infinity and leave behind flat space. As an example let us consider the evolution of a centered wave with $A = 1$. For these initial data the Kretschmann scalar,

$$I = C_{abcd}C^{abcd}, \quad (12)$$

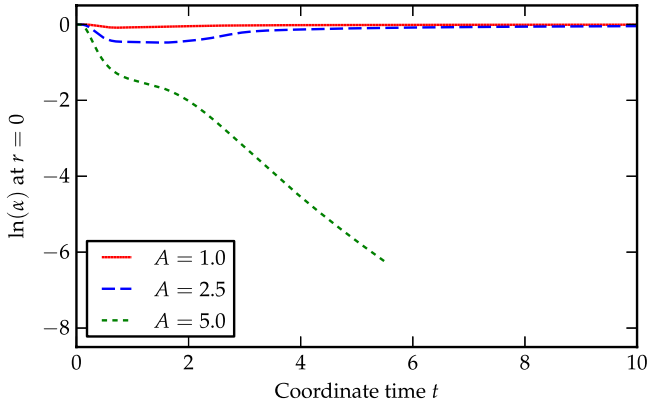

FIG. 1 (color online). The central value of the lapse as a function of time for Brill waves with $\rho_0 = 0$, evolved with moving-puncture gauge conditions. We show results for different values of A. For weak-field initial data with $A = 1$, the wave disperses to spatial infinity and leaves behind flat space, as expected. For larger values of A, however, our simulations develop discontinuities in the metric functions, which spoil the further evolution of the wave.

with the Weyl tensor $C_{abcd} = R_{abcd}$ in vacuum, takes its maximum value of ≈ 216 at the origin. We evolve with $\mu_S = 1$ and $\eta = 3 \approx 1/(10M)$ in the Gamma-driver condition (8), and find that, at the origin, the lapse function decreases initially, but quickly moves back toward unity. In Fig. 1 we compare this behavior with that for other amplitudes. The initial pulse in the Kretschmann scalar disperses away and leaves behind $I = 0$, indicating that the space is flat.

Evolution of $A = 2.5$ centered Brill data: For larger, but still subcritical A, the waves will interact nonlinearly before dispersing, but ultimately they still leave behind flat space. The Kretschmann scalar for centered Brill data with $A = 2.5$ takes its maximum at the origin, but now with a value of ≈ 2320. We evolved these data with $\eta = 2 \approx 2/(5M)$. The lapse at the origin again decreases at early times, this time to smaller values than for $A = 1$, and then returns to unity. The Kretschmann scalar also disperses to infinity, as before.

Evolution of $A = 5$ centered Brill data: For amplitudes larger than some critical $A_\star$ one expects black hole formation. For larger values of A our simulations are not successful, in the sense that we are not able to track the formation of an apparent horizon as it settles down to a Schwarzschild hole. We show more detailed results for $A = 5$ in Fig. 2, where profiles of the lapse function α, the metric component γ_{xx}, and trace K are plotted at different instants of time. The lapse collapses in the central region and develops a minimum along a ring of radius $r \approx 2.0$ in the equatorial plane in a simulation with $\eta = 11.4 \approx 8/M$. The metric simultaneously develops an increasingly large gradient across this ring, which ultimately turns into a discontinuity if we use $\eta = 0$ in the Gamma-driver condition (8). Associated with this gradient is a large

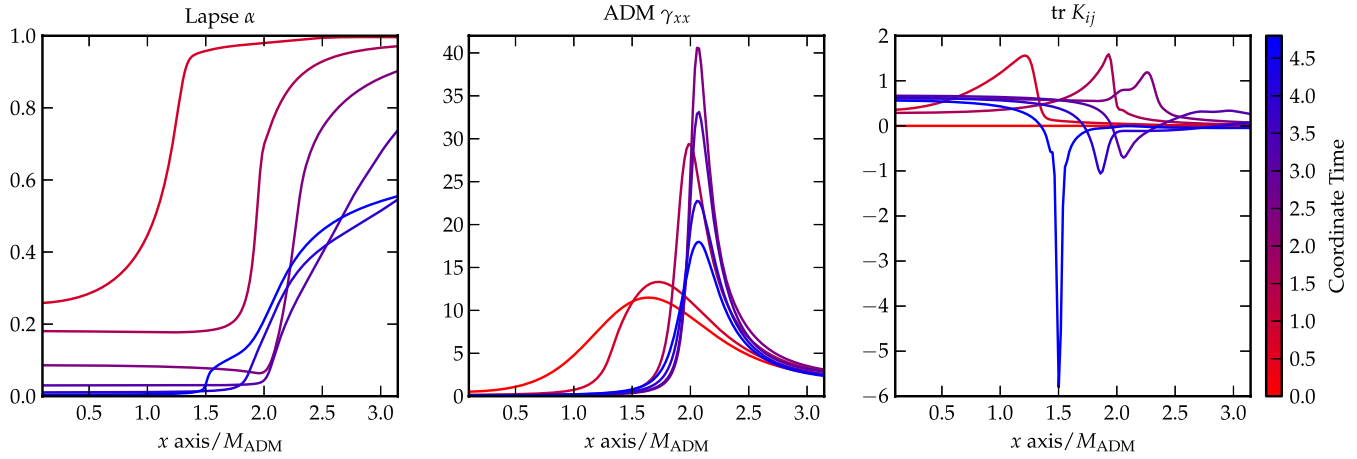

FIG. 2 (color online). Snapshots of the lapse function α (left panel), the ADM metric component γ_{xx} (center panel) and the trace of the extrinsic curvature trK_{ij} at different instants of time, for $A = 5$. We show all quantities along the x axis, with time indicated by hot-to-cold colors. The lapse develops a minimum on a ring of radius $r \approx 2.0$, which then travels toward the origin. The spatial metric develops a large gradient around the same ring. A sharp feature at radius $r \approx 1.5$ appears in the lapse, and K diverges around the same place. The latter feature is not visible in the metric.

numerical error that can be seen, for example, in the violation of the constraints. A pulse in the lapse then approaches the origin, so that the region with a nearly vanishing lapse becomes smaller. As this happens the trace of the extrinsic curvature at the incoming lapse pulse becomes large, negative, and sharp, ending in a numerical failure that we believe is a coordinate singularity. Similar behavior has been observed with the 1 + log gauge elsewhere; see for example [40]. Furthermore, we were able to reproduce this failure in the spherical code used to develop the Z4c formulation [41–45] by evolving flat space with a perturbed initial lapse with precisely the gauge of the Brill wave evolutions. This feature causes the numerical approximation to fail at around $t = 5.5$. Curiously here, in preliminary tests, we found that mesh refinement can cause problems. Often coarser grids are used to push the outer boundary far away inexpensively. But we found that the solutions being constructed are so extreme that if the grids are too coarse then they will fail during the single Runge-Kutta time step needed before the data from the finer boxes can be used to overwrite coarse grid data.

Discussion, comparison with the literature: The basic picture is similar to other nonlinear dynamical systems for which the strength of the initial fields is controlled by a parameter A, which separates two distinct states at some critical value $A_\star$. Near this value such systems may display critical behavior, as reviewed elsewhere [20,21]. For vacuum spacetimes, critical collapse was first reported by [23,24], who used Teukolsky data. To the best of our knowledge, all published results since then have adopted Brill initial data (see Table I). Only one author, Sorkin [30], has reported critical phenomena for Brill data, and even those simulations required significant fine-tuning of parameters in the gauge conditions. The study also reports qualitative differences from the earlier work; in particular, [30] finds that a spacetime singularity forms on a ring of nonzero radius in the equatorial plane, while for the simulations of [23,24] the singularity formed centrally. Finally, Sorkin reports a critical value of $A_\star \sim 6.27$, in contrast to smaller values found in earlier studies, for example $A_\star \sim 4.76$ in [28]. The size of the difference is puzzling. Unfortunately, since we have not been able to evolve large data reliably with the moving-puncture gauge, we cannot shed any light on the issue here.

Summary: We conclude that moving-puncture coordinates are not suitable for the evolution of the Brill waves considered in this section. For several other coordinate choices, including maximal slicing for the lapse, as well as quasi-isotropic or zero shift, it also appears to be difficult to obtain sufficiently reliable simulations that allow the study of critical phenomena in the vicinity of the critical amplitude. We know from other studies that moving-puncture coordinates can be used in collapse scenarios, so rather than altering the gauge choice we will study evolutions of different initial gravitational wave data.

B. Teukolsky waves

Initial data: Linear solutions to Einstein's equations describing quadrupolar gravitational waves can be constructed from a seed function

$$F(r, t) = F_1(t - r) + F_2(t + r), \tag{13}$$

where F_2 describes an outgoing solution while F_1 describes an ingoing solution (see [19]; see also Sec. 9.1 in [38]; see also [46] for a generalization to all multipoles). We choose $F_1 = -F_2$ so that the resulting solution exhibits a moment of time symmetry, and hence $K_{ij} = 0$, at $t = 0$. We then choose

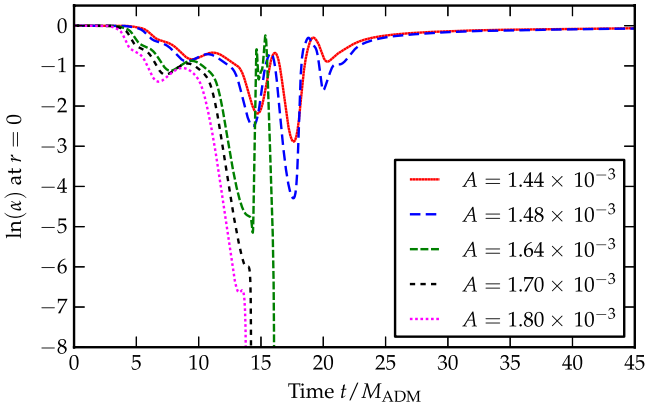

FIG. 3 (color online). The central value of the lapse as a function of time for Teukolsky waves with $r_0 = 2$ and $\sigma = 1/2$, evolved with moving-puncture gauge conditions. We show results for different values of A. For subcritical initial data with $A < A_\star \approx 0.0015$, the wave disperses to spatial infinity and leaves behind flat space, while for $A > A_\star$ the fields collapse to form a black hole.

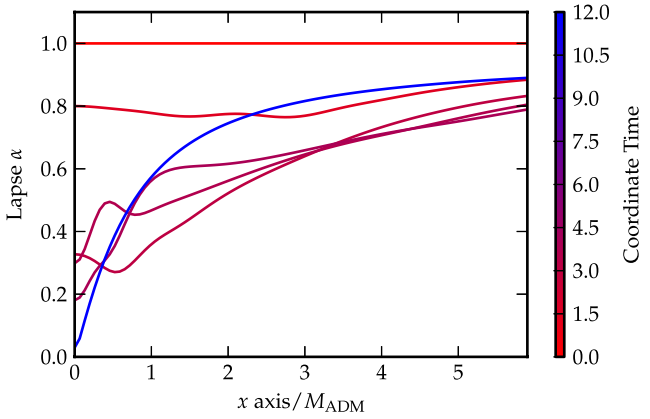

FIG. 4 (color online). Profiles of the lapse function α for a Teukolsky wave with amplitude $A = 0.0018$. Even though at early times the lapse forms a minimum at finite radius r, it ultimately collapses most rapidly at the center. This behavior is qualitatively different from the behavior of the lapse in the collapse of a Brill wave, as shown in the top panel of Fig. 2.

$$F_1(u) = \frac{A}{2}\left(\frac{u}{\sigma} e^{-((u+r_0)/\sigma)^2} + \frac{u}{\sigma} e^{-((u-r_0)/\sigma)^2}\right) \quad (14)$$

with $u \equiv t - r$. Here A is again a measure of the wave's amplitude, σ of its wavelength, and ρ_0 of the center of the original wave. Following the prescription in [19] we construct the spatial metric γ_{ij} for a quadrupolar ($\ell = 2$), $m = 0$ wave from the seed function (14). The resulting metric satisfies Einstein's equations to linear order in A. To construct true initial data from the above solution we only need to solve the Hamiltonian constraint, since the momentum constraint (3) is satisfied identically by time-symmetric data. We do so by adopting the above metric at $t = 0$ as a conformally related metric $\bar{\gamma}_{ij}$ and solving the Hamiltonian constraint (6) for the conformal factor ψ. Following [23,24] we consider "noncentral" initial data, i.e. wave packets that are initially centered on a positive radius r_0. Specifically, we choose $r_0 = 2$ and $\sigma = 1/2$ for all simulations presented in this section.

Evolution of Teukolsky data: For a given choice of σ and r_0, the spacetime again depends only on the amplitude A, although the specifics of the evolution will of course depend upon the gauge. Time-symmetric initial data represent a superposition of interacting ingoing and outgoing waves. At the amplitudes we consider, the interaction of these waves is weak. The outgoing wave travels toward infinity and does not play an important role in our simulations. The ingoing wave, on the other hand, travels toward the origin. For sufficiently small initial amplitudes the time evolution is well approximated by the analytical, linear solution. If the amplitude is smaller than a certain critical value $A_\star$ we again expect that the evolution ultimately leaves behind flat space, possibly after interacting in a nonlinear fashion. For $A > A_\star$ the waves collapse to form a black hole. Note that the wave's amplitude increases as it travels from r_0 to the origin, so that we expect $A_\star$ to be smaller for noncentral initial data than for similar "central" initial data. We perform evolutions with moving-puncture coordinates. Our expectations for small initial data are borne out in practice, so we will not comment further.

Numerical evolution of supercritical data: The main result of this work is that we are able to evolve Teukolsky wave initial data through black hole formation. As an example of such a supercritical evolution we focus on results for $A = 0.0018$. As shown in Fig. 3, the central value of the lapse exhibits several large-amplitude oscillations, but ultimately approaches zero at the center, indicating the formation of a black hole. In Fig. 4 we show profiles of the lapse at different instances of time. At early times, the lapse takes a minimum at finite radius, but at later times it collapses most rapidly at the center. This behavior should be compared with what we found for Brill waves, for which the lapse always collapses most rapidly at a finite radius (see the top panel in Fig. 2). The peak of the curvature scalar occurs at the origin. We found that an apparent horizon forms at $t \approx 4.2$. In Fig. 5 we show the "world tube" of this horizon in a spacetime diagram.

Collapse to a black hole and horizon formation: Our initial data are axisymmetric, but carry no angular momentum. Therefore, if a black hole forms in the time evolution of these initial data, this black hole must ultimately settle down into a Schwarzschild black hole. However, since the initial data are not spherically symmetric, the newly formed black hole may also deviate from spherical symmetry. We then expect that these deviations from spherical symmetry lead to quasinormal oscillations in the horizon that damp away and leave behind a Schwarzschild black hole. This behavior can be observed in the horizon's world

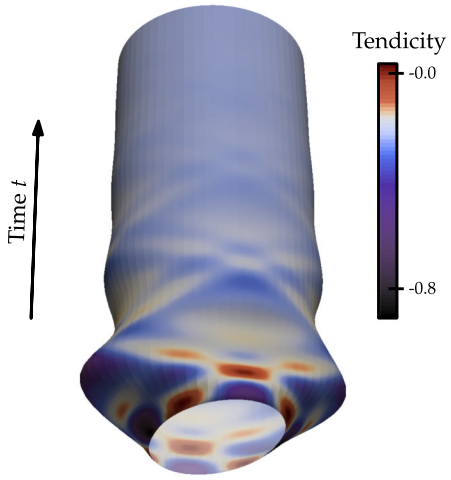

FIG. 5 (color online). A "world tube" showing the newly formed horizon in the collapse of a Teukolsky wave for $A = 0.0018$. For each instant of time we show a ring that represents the coordinate location of the horizon along lines of constant longitude, going from one pole to the other and back. Connecting these rings for different times results in the cylinderlike shape shown in the figures. The shape of this cylinder demonstrates the horizon's initial quasinormal oscillation, while the color coding shows the horizon's tendicity $\mathcal{E}_{NN}M^2$. After a few oscillations the horizon settles down into that of a static Schwarzschild black hole.

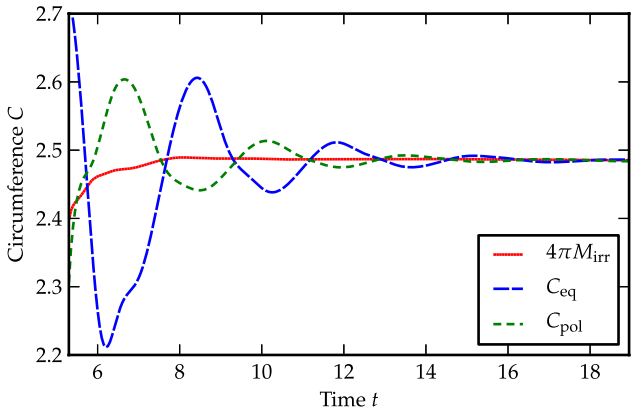

FIG. 6 (color online). The equatorial and polar proper circumference of the newly formed horizon of a Teukolsky wave for $A = 0.0018$. Also included is the irreducible mass $M_{\rm irr}$, multiplied by 4π, which equals the proper circumference of a spherically symmetric Schwarzschild black hole [see Eq. (15)]. The initially formed black hole is not spherical, but oscillates and settles down into a Schwarzschild black hole. During the initial oscillation the irreducible mass of the black hole still increases by a few percent.

tube in Fig. 5, which clearly shows these initial oscillations with a rapidly decreasing amplitude, leaving behind a spherical horizon at late times. We note, however, that Fig. 5 only shows the coordinate location of the horizon, which does not have an immediate physical meaning. As a (spatial) coordinate-independent measure of the horizon's deviation from spherical symmetry we plot its equatorial and polar proper circumferences in Fig. 6. Both circumferences perform a damped oscillation, almost exactly out of phase, and, as expected, settle down to the same, time-independent value. The circumference of a Schwarzschild black hole is given by

$$C = 2\pi R = 4\pi M, \tag{15}$$

where $R = 2M$ is the circumferential radius of a Schwarzschild black hole. We therefore include the value $4\pi M_{\rm irr}$ in Fig. 6, where we compute the black hole's irreducible mass $M_{\rm irr}$ from the proper area of its apparent horizon. Figure 6 shows that both the polar and equatorial proper circumferences settle down to the Schwarzschild circumference, demonstrating that the initially distorted black hole settles down to the trumpet geometry. The fact that the late-time horizon takes a spherical shape even in coordinate space, as seen in Fig. 5, demonstrates that the Gamma-driver shift condition (8) allows the coordinate evolution to reflect the spherical symmetry of the spacetime.

Horizon tendicity: As an alternative (spatial) coordinate-independent measure of the horizon geometry we compute its tendicity,

$$\mathcal{E}_{NN} \equiv \mathcal{E}_{ij}s^i s^j, \tag{16}$$

where $\mathcal{E}_{ij}$ is the electric part of the Weyl tensor, and s^i the spatial unit normal on the horizon (see [47–49]; see also [50] for an analytical demonstration). For a Schwarzschild black hole the tendicity is

$$\mathcal{E}^{\rm SS}_{NN} = -\frac{1}{4M^2} \tag{17}$$

(see, e.g., [47,50]). In Fig. 5 we have indicated the horizon tendicity using a color coding. At early times, the tendicity varies significantly across the horizon, meaning that the horizon is significantly distorted, while at late times the tendicity becomes increasingly uniform across the horizon, with a value close to the analytical value (17) for a Schwarzschild black hole. As the newly formed black hole performs quasinormal oscillations, deviations of the tendicity from its average value propagate across the horizon in a wavelike manner, from the poles to the equator and back. This can be seen in the color-coding in Fig. 5. For a detailed analysis of quasinormal modes using the tendex-vortex formalism, see [49].

Approach to a trumpet slice: To complete this section we analyze the late-time solution to which our dynamical evolutions settle down. Given that we use moving-puncture coordinates, we expect that a black hole settles down into a trumpet geometry [10,12,13,51]. To compare results with the analytical solutions for a maximally sliced trumpet solution [51], we show in Fig. 7 results for an evolution with the "nonadvective" version of the 1 + log slicing (7) and Gamma-driver (8) [we also used $\mu_S = 3/4$ and $\eta = 0$ in (8) for these simulations]. In Fig. 7 we show a snapshot of the lapse at time $t = 15.8$ and compare our numerical

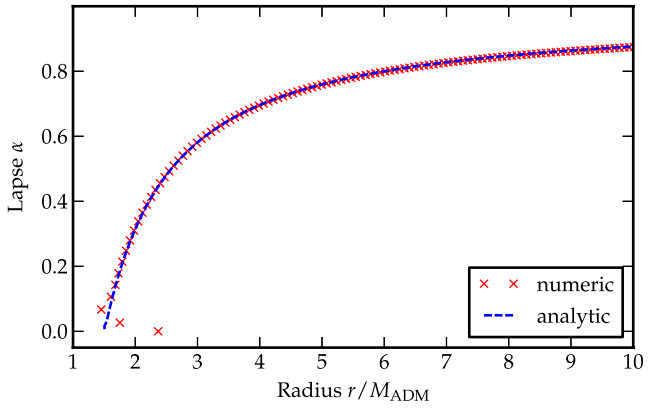

FIG. 7 (color online). Radial profile of the lapse α for the collapse of a Teukolsky wave with $A = 0.0018$, at time $t = 15.8$ (crosses). This evolution is carried out with "nonadvective" $1 + \log$ slicing, so that we can easily compare with the analytical solution for a maximally sliced trumpet solution (solid line). Note that the overall scale of the analytical solution for the lapse is set by the boundary condition at $r = \infty$. The numerical solution, however, results from the collapse of nonlinear wave initial data and is not affected by the boundary condition at spatial infinity; accordingly, the overall factor of the solution for the lapse may be different. Here we found excellent agreement by multiplying the analytical solution with a factor of 0.98. The innermost few grid points are affected by numerical noise that results from finite differencing across the singularity at $r = 0$.

results with the analytical results of [51]. We plot the lapse as a function of areal radius R in order to compare gauge-invariant quantities. The agreement is excellent, after an overall scale factor has been adjusted. This scale factor allows for the fact that the analytical solution assumes that the lapse approaches unity at spatial infinity, while our dynamical simulations do not impose this condition. We compare numerical and analytical values for the shift and find similarly good agreement.

Experiments near the critical region: As we increase the amplitude from 0, we observe increasingly large and rapid oscillations. This can be seen in Fig. 3, where we show central values of the lapse as a function of time for different values of the amplitude A. For the simulations shown in Fig. 3 we adopted the moving-puncture coordinates (7) and (8) with $\eta \approx 2/M_{\rm ADM}$. We experimented with the nonadvective version of the $1 + \log$ slicing condition (7) and found similar results. We summarize our results in Table II, where we list the initial Arnowitt-Deser-Misner (ADM) mass and the irreducible mass of the black hole if such a black hole forms. As can be seen in Table II and Fig. 3, the critical value of the amplitude is between $A = 0.00148$ and $A = 0.00164$. For $A > A_\star$ the lapse ultimately collapses to zero at the center. For both sub- and supercritical values of the amplitude, the lapse exhibits more and larger oscillations before returning to unity or collapsing to zero for amplitudes closer to the critical value. This behavior is an indication of the critical behavior in the vicinity of the critical amplitude.

TABLE II. Summary of results for nonlinear Teukolsky waves with different initial amplitude A. The amplitudes $A = 0.00148$ and $A = 0.00164$ are, respectively, the highest subcritical and lowest supercritical data we tried that did not fail. We tabulate the irreducible mass $M_{\rm irr}$ of the black hole, if a black hole formed in the evolution, the initial ADM mass $M_{\rm ADM}$, and the ratio between the two. The irreducible mass increases while the initially formed black hole settles down into equilibrium (compare Fig. 6); we list here the near-equilibrium value after several oscillation periods.

A	$M_{\rm irr}$	$M_{\rm ADM}$	$M_{\rm irr}/M_{\rm ADM}$
0.00140	...	0.222	...
0.00142	...	0.229	...
0.00144	...	0.236	...
0.00146	...	0.243	...
0.00148	...	0.250	...
0.00164	0.144	0.312	0.460
0.00166	0.151	0.321	0.470
0.00168	0.158	0.329	0.480
0.00170	0.164	0.338	0.513
0.00175	0.181	0.360	0.550
0.00180	0.197	0.383	0.584
0.00200	0.265	0.486	0.737

Summary: We conclude that, at least for amplitudes not too close to the critical amplitude, moving-puncture coordinates are well suited to simulate the evolution of Teukolsky waves. For subcritical waves we follow the nonlinear interaction of the waves and their dispersal to spatial infinity, while for supercritical waves we track their implosion, detect the formation of apparent horizons, and follow the evolution of the newly formed black holes as they settles down to spherical symmetry. For amplitudes close to the critical amplitude our codes fail. We believe that this is caused by the lack of sufficient resolution as, close to the critical amplitude, the dynamical evolution leads to increasingly small features.

IV. CHARACTERIZATION OF INITIAL DATA

Evolving Brill and Teukolsky waves in Sec. III we found that Teukolsky data can be evolved with moving-puncture coordinates without problems—except, possibly, in the immediate proximity of the critical point—whereas Brill data are more troublesome. While it is difficult to pinpoint what exactly creates this difference in behavior, we offer some speculations on the causes of these differences in this section. An obvious set of questions presents themselves. The Brill data were centered at the origin, whereas the Teukolsky data were not. Could this be the cause of the difference? Are the two types of data somehow geometrically different? If so, would this difference be maintained in time evolution, and can we modify the Brill data to make it more amenable to numerical

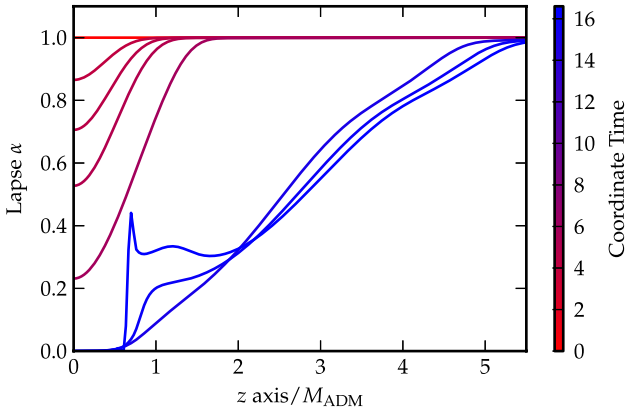

FIG. 8 (color online). Profiles of the lapse at different instances of time along the z axis for an off-centered Brill wave with $A = 0.12$ and $\rho_0 = 4.0$. Initially the lapse collapses at the center. At late times of the evolution, a gauge pulse is traveling in and gets blueshifted. At the interface between the collapsed lapse and the gauge pulse, a coordinate singularity appears. This leads to a failure of the simulation.

evolution with the moving-puncture gauge? We address each of these issues in turn.

A. Off-center Brill wave evolutions

Small data: We evolve two sets of weak, off-center Brill wave initial data with offset $\rho_0 = 4$ in (11). Specifically, we choose data with amplitudes $A = 0.053$ and $A = 0.0815$, which have ADM masses ≈ 0.59 and ≈ 1.4, respectively. For the weaker $A = 0.053$ data we use $\eta \approx 1/M$, while for $A = 0.0815$ we chose $\eta \approx 2/M$. As for earlier weak Brill data we found that both waves disperse after a brief interaction around the origin. For the weaker data, the Kretschmann scalar takes a maximum value ≈ 48 at the origin, while for the stronger data the maximum is ≈ 200, again at the origin.

Large data: We now take the same offset but $A = 0.12$, which makes the ADM mass ≈ 3.15. We used $\eta = 8/M$. As in the "small data" tests, the lapse initially decreases most rapidly around the peak of the seed function in the xy plane. It then decreases to zero near the origin. Then an incoming gauge wave travels along the z axis toward the origin. Since the speed of the gauge wave is $\sim\sqrt{2\alpha}$, and travels from a region with $\alpha \sim 1$ to one with $\alpha \sim 0$, there is a rapid blueshift effect; the solution becomes badly resolved. At some point in time, around the interface of these two regions, the trace of the extrinsic curvature becomes negative, which leads to an increase in the lapse [see Eq. (7)]. Ultimately, this results in a coordinate singularity causing the code to fail at $t \approx 16$. We note a remarkable similarity between the lapse profile we obtain, shown in Fig. 8, and that shown in Fig. 2 of [40] where such coordinate singularities were studied in evolutions of flat space. We conclude that, for sufficiently large amplitudes, moving-puncture coordinates fail even for off-centered Brill wave initial data.

B. Axisymmetric twist-free, time symmetric data

Harmonic spatial coordinates: We start by searching for differences in the geometry of Brill and Teukolsky waves. In cylindrical coordinates, the conformally related metric for Brill wave initial data is given by

$$\bar{\gamma}_{ij} = \begin{pmatrix} e^q & 0 & 0 \\ 0 & e^q & 0 \\ 0 & 0 & \rho^2 \end{pmatrix} \tag{18}$$

[see Eq. (9)], whereas for Teukolsky waves the conformally related metric takes the form

$$\bar{\gamma}_{ij} = \begin{pmatrix} \bar{\gamma}_{\rho\rho} & \bar{\gamma}_{\rho z} & 0 \\ \bar{\gamma}_{\rho z} & \bar{\gamma}_{zz} & 0 \\ 0 & 0 & \bar{\gamma}_{\phi\phi} \end{pmatrix}. \tag{19}$$

Evidently, the two data sets are given in different coordinate systems, and a meaningful comparison can only be made once they have been expressed in the same coordinates. However, any axisymmetric, twist-free metric can be brought into the form

$$\bar{\gamma}_{ij} = \begin{pmatrix} e^q & 0 & 0 \\ 0 & e^q & 0 \\ 0 & 0 & \rho^2 V \end{pmatrix}, \tag{20}$$

in some coordinate system (ϱ, ξ, ϕ). Crudely speaking, this is possible because the two-metric in the ρ-z subspace can always be brought into an explicitly conformally flat form [[52], Ch. 3, Ex. 2].

Geometrically oblate and prolate initial data: Any spherically symmetric metric can be brought into the form (20) with $V = e^q$. For our gravitational wave initial data, which are not spherically symmetric, V will, in general, be different from e^q. Evidently, deviations of V from e^q can be produced in two ways: either $V > e^q$ or $V < e^q$. We characterize data with $V > e^q$ as *geometrically oblate* and data with $V < e^q$ as *geometrically prolate*. We use the word "geometrically" to distinguish the terminology from that normally used with Brill waves, where the word oblate or prolate applies to the seed function. Clearly, both V and e^q are functions of the coordinates, so that data may be geometrically oblate in some region and prolate in another. We also point out that we apply this characterization only to the initial data; it is not evident whether or how this characterization is maintained during a time evolution, even if the data are globally geometrically oblate or prolate initially. The characterization as geometrically oblate or prolate may nevertheless be a useful distinction between the geometries of Brill and Teukolsky data evolved earlier. An example of initial data of a certain character that is maintained is given in [53].

Geometric oblateness of Brill and Teukolsky data: For the Brill wave initial data of Sec. III A we have $V = 1$; moreover we chose a positive amplitude A in the seed

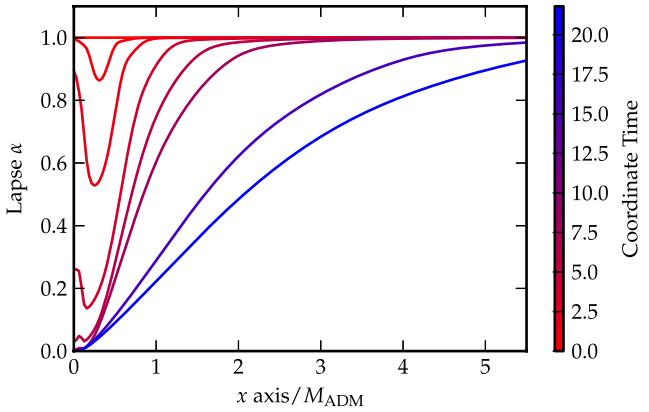

FIG. 9 (color online). Profiles of the lapse at different instances of time for a negative-amplitude, centered Brill wave with $A = -5$. These profiles should be compared with (a) those of a positive-amplitude Brill wave in the top panel in Fig. 2, and (b) those for a Teukolsky wave in Fig. 4.

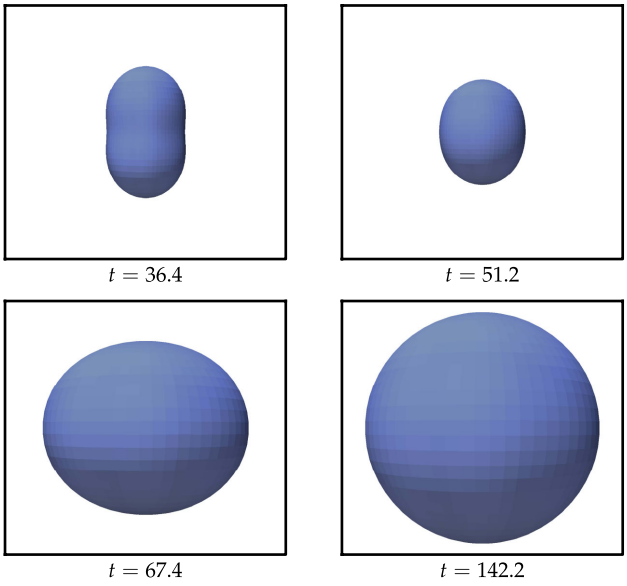

FIG. 10 (color online). Snapshots of the apparent horizon for supercritical off-center geometrically oblate Brill waves. The apparent horizon is first discovered at $t = 36.4$ and has a peanut-like shape, where in the plots the z axis runs vertically. The subsequent frames show the oscillations of the horizon, which jumps at $t \approx 65$.

function (11), which results in $e^q \geq 1$. This means that the Brill wave initial data of Sec. III A are geometrically prolate everywhere except on the z axis. For Teukolsky waves the classification is less obvious, because it requires an additional coordinate transformation. Interestingly, however, Fig. 3 in [24] shows that the geometry close to the center is geometrically oblate. (The quantity e^η used by [24] is a measure of the ratio e^q/V; the fact that their η is negative in a region around the origin implies that the geometry is oblate there.) This observation could point to a fundamental difference in the geometries of $A > 0$ Brill and Teukolsky waves.

Discussion: These arguments are neither rigorous nor complete, but they lead to an immediate suggestion: if it were true that geometrically oblate data are better behaved in dynamical evolutions than prolate data—for example in the sense that they form a singularity at the center rather than on a ring—then it would be of interest to produce geometrically oblate Brill wave initial data. We consider such data next.

C. Negative-amplitude Brill waves

Geometrically oblate Brill waves: In this section we consider geometrically oblate Brill wave data. Such data can be produced in exactly the same way as the prolate data in Sec. III A, by adopting negative amplitudes $A < 0$ in the seed function (11).

Centered geometrically oblate Brill waves: We evolved three sets of initial data with $\rho_0 = 0$ and $A < 0$, namely $A = -1$, $A = -2.5$, and $A = -5$, with ADM masses of approximately 0.61, 1.37, and 3.15, respectively. As in the geometrically prolate case, the first two data sets just allow the Kretschmann scalar to propagate away, taking maximal values of about 56 and 1072 appearing at the origin. For the stronger field evolution the numerics again eventually fail, although now at around $t = 22.5$. In Fig. 9 we show profiles of the lapse at different instances of time for such a Brill wave with $A = -5$. Interestingly, these profiles are qualitatively different from those for the geometrically prolate, positive-amplitude Brill waves shown in the top panel of Fig. 2. While for geometrically prolate Brill waves the lapse always takes a minimum at finite radius, which we found to coincide with the development of increasingly large gradients in the spatial metric, for negative-amplitude Brill waves the lapse ultimately takes a minimum at the center. This is the same behavior that we highlighted for Teukolsky waves in Fig. 4. We were able to follow the collapse of geometrically oblate Brill wave past black hole formation, and in contrast to positive-amplitude Brill waves we were also able to locate apparent horizons, at least in the spherical coordinate code [54]. However, at least with the setup we chose, the BAM apparent horizon finder did not give reliable results. At late times, steep gradients in the metric functions again appeared, but this time well inside the horizon, close to the center. Ultimately, these gradients spoil further numerical evolution.

Off-center geometrically oblate Brill waves: We again evolved three sets of initial data $A = -0.044$, $A = -0.061$, and $A = -0.08125$, all with $\rho_0 = 4$. The ADM masses of these spacetimes are approximately 0.61, 1.36, and 3.15 with peak values of the Kretschmann scalar initially around 64, 108, and 88, respectively. It is interesting that the "larger" initial data do not have the largest initial Kretschmann, but the evolution leaves no doubt that the $A = -0.08125$ data are indeed the stronger. As in our previous results the two weaker data sets leave behind $I = 0$, with greater oscillations

in the Kretschmann scalar in the $A = -0.061$ case. The maximum of the Kretschmann scalar in the evolution of the $A = -0.044$ is around 19 and occurs at the origin at $t \simeq 7.4$. Likewise with the $A = -0.061$ data, the maximum occurs at the origin, with a value around 373 at $t \simeq 12$. In both the $A = -0.044$ and the $A = -0.061$ evolutions the Kretschmann scalar propagates away predominantly along the symmetry axis. We evolved the strongest data $A = -0.08125$ set in the BAM code until $t = 150$. It collapses to form a black hole similar to the Teukolsky data presented in Sec. III B. An apparent horizon was first discovered at $t = 36.4$. In Fig. 10 some snapshots of the evolution of the horizon are plotted. The apparent horizon mass eventually settles down to $M = 1.73$. Comparing the maximum resolution in this simulation relative to this scale with the earlier Teukolsky wave BAM evolution for $A = 0.00175$, the present data have roughly 9 times the resolution, which may explain why we did not obtain reliable results from the BAM apparent horizon finder earlier. So by choosing the parameters in the Brill wave data carefully we can obtain evolutions comparable to those we had with Teukolsky initial data.

V. SUMMARY

We presented numerical simulations of nonlinear gravitational waves. We adopted two different types of initial data—Brill and Teukolsky waves—and evolved them with two independent numerical codes.

We consistently find that positive amplitude Brill waves, most commonly evolved in the literature, fail to produce long-term stable evolutions with the moving-puncture gauge, unless the initial amplitude is small. Evolving these data with this gauge leads to steep gradients in metric functions, which ultimately spoil the numerical evolution. Comparing with earlier studies it seems most likely that the failure is a coordinate singularity. For positive-amplitude Brill waves we are also unable to locate black hole horizons, even for data that we believe do form black holes.

On the other hand, we find that Teukolsky waves do allow a stable, long-term evolution in moving-puncture coordinates, unless the initial amplitude is close to critical. We followed the evolution of the waves and their collapse to a black hole, tracking the newly formed horizon, and confirming that the spatial slices settle down to a trumpet geometry.

The primary motivation was therefore to provide one more example of successful simulations with moving-puncture coordinates that track the collapse of regular initial data to a black hole. Another motivation is to point out the surprising, qualitative differences between Brill and Teukolsky wave initial data. We speculate that the choice of initial data has significantly contributed to the fact that the original studies of criticality in the collapse of nonlinear waves [24] have been so difficult to reproduce. In retrospect, it is surprising that none of the studies after [24] considered Teukolsky waves. Apart from choosing Brill waves for technical convenience, this may appear justified because critical phenomena are not expected to depend on details of the initial data, which is an aspect of universality found in many studies. However, wave collapse in axisymmetry also marks a departure from spherical symmetry often used in other studies. Axisymmetry opens up the possibility that new geometric aspects matter, and the present study is an example.

Our findings also raise new questions. In particular, it would be desirable to understand why Brill and Teukolsky waves behave so differently. We discussed a characterization of twist-free, axisymmetric data as geometrically either prolate or oblate. While this characterization does point to qualitative differences in the respective geometries, our analysis is incomplete in the sense that it does not consider the time dependence of the characterization. We believe that it would be worthwhile to further pursue this or similar approaches in order to gain a deeper insight into the geometries of these waves. On the basis of this characterization, as an attempt to make the Brill wave data as close as possible to the Teukolsky evolutions, we evolved off-center negative amplitude Brill waves. We found that we were once again able to evolve such data through apparent horizon formation, and furthermore as they settle down to a Schwarzschild black hole.

Unfortunately, our simulations still break down, even for Teukolsky waves, in the most interesting regime, namely close to the critical amplitude. This prevents us from analyzing critical phenomena with our current simulations. We believe that this failure occurs because of the lack of sufficient spatial grid resolution. As one approaches the critical point, the evolution leads to oscillations on increasingly small scales. At least with moving-puncture coordinates, the underresolution of these oscillations causes the lapse to become negative, which then spoils the numerical evolution. The need for increasingly fine spatial resolution in the vicinity of the critical point is not a new revelation, of course; it explains, for example, why a well-adjusted adaptive grid refinement proved so crucial in the original simulations of Choptuik [22]. We also cannot exclude the possibility that the moving-puncture coordinates themselves fail close to the critical point, irrespective of resolution. In either case, we plan to develop techniques (for example unequal grid spacing in our spherical-coordinate code), and experiment with the slicing and gauge conditions, in order to study critical phenomena in the collapse of nonlinear waves in the future.

ACKNOWLEDGMENTS

We are grateful to David Garfinkle for very interesting discussions. T. W. B. gratefully acknowledges support from the Alexander-von-Humboldt Foundation and would like to thank the Max-Planck-Institut für Astrophysik for its hospitality. This work was supported in part by the Deutsche Forschungsgemeinschaft (DFG) through its Transregional Center SFB/TR7 "Gravitational Wave

Astronomy," by NSF Grant No. PHY-1063240 to Bowdoin College, by the DFG Research Training Group 1523/1 "Quantum and Gravitational Fields," by the Graduierten-Akademie Jena, and by the Spanish Ministry of Science through Grant No. AYA2010-21097-C03-01. Computations were performed primarily at the LRZ (Munich).

APPENDIX: NUMERICS

The numerical results presented in this paper were produced with two different numerical codes. Both of these codes evolve Einstein's equations in the BSSN formulation [4–6] using finite-difference methods, but in completely independent implementations.

The BAM *code:* One of our codes is the BAM code, which adopts Cartesian coordinates and is described in [45,55–57]. The evolutions in this paper were performed with an explicit fourth-order Runge-Kutta method and fourth-order finite differences for the spatial derivatives. Mesh refinement is provided by a hierarchy of cell-centered nested Cartesian grids and Berger-Oliger time stepping. Metric variables are interpolated in space by means of sixth-order Lagrangian polynomials. Interpolation in Berger-Oliger time stepping is performed at second order. In Fig. 11 we show a convergence test for a Brill wave with positive amplitude $A = 5$.

The spherical-polar coordinate code: Our other code is an implementation of BSSN in spherical polar coordinates [54]. The code adopts a reference-metric formulation of the BSSN formalism [58], uses a partially implicit Runge-Kutta method for the time evolution [59,60], and scales out appropriate factors of r and $\sin\theta$ from all tensorial quantities. Spatial derivatives are evaluated using fourth-order finite differencing, except for advective (shift) terms, which are evaluated to third order. Our current implementation differs from that described in [54] in that it now uses a third-order finite differencing for the advective terms (rather than second order), in that we have implemented an apparent horizon finder using the approach of [61,62], and in that we now use trilinos software [63,64] to solve elliptic equations. While this code does not make any symmetry assumptions, the axisymmetric solutions considered in this paper can be computed efficiently by choosing the minimum number of grid points possible in the ϕ direction.

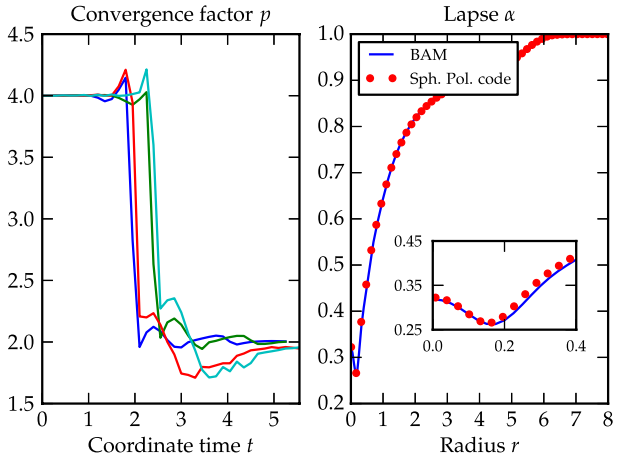

FIG. 11 (color online). In the left panel self-convergence tests for the $\chi = \psi^{-4}$ variable are plotted from the BAM data. A centered Brill wave with $A = 5$ is evolved using four different resolutions. The red lines shows the self-convergence factor comparing 170, 227, and 340 spatial points along the axes in one of the mesh-refinement boxes with $x_{\max} = 8.7$. For the blue line we use 227, 340, and 680 points along the axes. Initially the simulation shows fourth-order convergence. Note that the Berger-Oliger time interpolation at the mesh refinement boundary is done at second order, and may become the dominant error when evolving strongly dynamic waves. Evidence for this is given by the green and turquoise lines, in which the convergence test is performed in a slightly smaller part of the grid. In the right panel a comparison between the numerical results obtained with our two codes, for a Teukolsky wave with amplitude $A = 0.0018$, is plotted. We show the lapse function α at time $t \approx 3.0$ as a function of r in the equatorial plane. The inset shows detail around the turning point.

Comparison: The codes produce consistent results. As an example, we compare in Fig. 11 the lapse function α in the equatorial plane at a time $t \approx 3$ for a collapsing Teukolsky wave.

[1] F. Pretorius, Phys. Rev. Lett. **95**, 121101 (2005).
[2] M. Campanelli, C. O. Lousto, P. Marronetti, and Y. Zlochower, Phys. Rev. Lett. **96**, 111101 (2006).
[3] J. G. Baker, J. Centrella, D.-I. Choi, M. Koppitz, and J. van Meter, Phys. Rev. D **73**, 104002 (2006).
[4] T. Nakamura, K.-i. Oohara, and Y. Kojima, Prog. Theor. Phys. Suppl. **90**, 1 (1987).
[5] M. Shibata and T. Nakamura, Phys. Rev. D **52**, 5428 (1995).
[6] T. W. Baumgarte and S. L. Shapiro, Phys. Rev. D **59**, 024007 (1998).
[7] C. Bona, J. Massó, E. Seidel, and J. Stela, Phys. Rev. Lett. **75**, 600 (1995).
[8] M. Alcubierre, B. Brügmann, P. Diener, M. Koppitz, D. Pollney, E. Seidel, and R. Takahashi, Phys. Rev. D **67**, 084023 (2003).
[9] J. R. van Meter, J. G. Baker, M. Koppitz, and D.-I. Choi, Phys. Rev. D **73**, 124011 (2006).
[10] M. Hannam, S. Husa, D. Pollney, B. Brügmann, and N. Ó. Murchadha, Phys. Rev. Lett. **99**, 241102 (2007).
[11] J. D. Brown, Phys. Rev. D **77**, 044018 (2008).

[12] M. Hannam, S. Husa, N. Ó. Murchadha, B. Brügmann, J. A. González, and U. Sperhake, J. Phys. Conf. Ser. **66**, 012047 (2007).
[13] M. Hannam, S. Husa, F. Ohme, B. Brügmann, and N. Ó. Murchadha. Phys. Rev. D **78**, 064020 (2008).
[14] B. Brügmann, Gen. Relativ. Gravit. **41**, 2131 (2009).
[15] L. Baiotti and L. Rezzolla, Phys. Rev. Lett. **97**, 141101 (2006).
[16] M. Thierfelder, S. Bernuzzi, D. Hilditch, B. Brügmann, and L. Rezzolla, Phys. Rev. D **83**, 064022 (2011).
[17] A. N. Staley, T. W. Baumgarte, J. D. Brown, B. Farris, and S. L. Shapiro, Classical Quantum Gravity **29**, 015003 (2012).
[18] D. S. Brill, Ann. Phys. (N.Y.) **7**, 466 (1959).
[19] S. A. Teukolsky, Phys. Rev. D **26**, 745 (1982).
[20] C. Gundlach, Living Rev. Relativity **2**, 4 (1999).
[21] C. Gundlach, Phys. Rep. **376**, 339 (2003).
[22] M. W. Choptuik, Phys. Rev. Lett. **70**, 9 (1993).
[23] A. M. Abrahams and C. R. Evans, Phys. Rev. D **46**, R4117 (1992).
[24] A. M. Abrahams and C. R. Evans, Phys. Rev. Lett. **70**, 2980 (1993).
[25] K. Eppley, in *Sources of Gravitational Radiation*, edited by L. L. Smarr (Cambridge University Press, Cambridge, 1979), pp. 275–291.
[26] M. Alcubierre, G. Allen, B. Brügmann, G. Lanfermann, E. Seidel, W.-M. Suen, and M. Tobias, Phys. Rev. D **61**, 041501(R) (2000).
[27] D. Garfinkle and G. Comer Duncan, Phys. Rev. D **63**, 044011 (2001).
[28] L. Santamaria, Master's thesis, Friedrich-Schiller-Universität Jena, 2006.
[29] O. Rinne, Classical Quantum Gravity **25**, 135009 (2008).
[30] E. Sorkin, Classical Quantum Gravity **28**, 025011 (2011).
[31] K. R. Eppley, Phys. Rev. D **16**, 1609 (1977).
[32] H. Friedrich, Commun. Math. Phys. **100**, 525 (1985).
[33] D. Garfinkle, Phys. Rev. D **65**, 044029 (2002).
[34] E. Sorkin, Phys. Rev. D **81**, 084062 (2010).
[35] R. Arnowitt, S. Deser, and C. W. Misner, in *Gravitation: An Introduction to Current Research*, edited by L. Witten (John Wiley, New York, 1962), pp. 227–265.
[36] J. W. York, Jr., in *Sources of Gravitational Radiation*, edited by L. Smarr (Cambridge University Press, Cambridge, 1979), pp. 83–126.
[37] M. Alcubierre, *Introduction to* 3 + 1 *Numerical Relativity* (Oxford University Press, New York, 2008).
[38] T. Baumgarte and S. Shapiro, *Numerical Relativity: Solving Einstein's Equations on the Computer* (Cambridge University Press, Cambridge, 2010).
[39] E. Gourgoulhon, 3 + 1 *Formalism in General Relativity* (Springer, Berlin, 2012).
[40] M. Alcubierre and J. Massó, Phys. Rev. D **57**, R4511 (1998).
[41] S. Bernuzzi and D. Hilditch, Phys. Rev. D **81**, 084003 (2010).
[42] M. Ruiz, D. Hilditch, and S. Bernuzzi, Phys. Rev. D **83**, 024025 (2011).
[43] A. Weyhausen, S. Bernuzzi, and D. Hilditch, Phys. Rev. D **85**, 024038 (2012).
[44] Z. Cao and D. Hilditch, Phys. Rev. D **85**, 124032 (2012).
[45] D. Hilditch, S. Bernuzzi, M. Thierfelder, Z. Cao, W. Tichy, and B. Brügmann, Phys. Rev. D **88**, 084057 (2013).
[46] O. Rinne, Classical Quantum Gravity **26**, 048003, (2009).
[47] R. Owen, J. Brink, Y. Chen, J. D. Kaplan, G. Lovelace, K. D. Matthews, D. A. Nichols, M. A. Scheel, F. Zhang, A. Zimmerman, and K. S. Thorne, Phys. Rev. Lett. **106**, 151101 (2011).
[48] F. Zhang, A. Zimmerman, D. A. Nichols, Y. Chen, G. Lovelace, K. D. Matthews, R. Owen, and K. S. Thorne, Phys. Rev. D **86**, 084049 (2012).
[49] D. A. Nichols, A. Zimmerman, Y. Chen, G. Lovelace, K. D. Matthews, R. Owen, F. Zhang, and K. S. Thorne, Phys. Rev. D **86**, 104028 (2012).
[50] K. A. Dennison and T. W. Baumgarte, Phys. Rev. D **86**, 084051 (2012).
[51] T. W. Baumgarte and S. G. Naculich, Phys. Rev. D **75**, 067502 (2007).
[52] R. M. Wald, *General Relativity* (*The University of Chicago Press*, Chicago, 1984).
[53] D. Christodoulou, *The Formation of Black Holes in General Relativity*, EMS Monographs in Mathematics Vol. 4 (European Mathematical Society Publishing House, Zürich, 2009).
[54] T. W. Baumgarte, P. J. Montero, I. Cordero-Carrión, and E. Müller., Phys. Rev. D **87**, 044026 (2013).
[55] B. Brügmann, J. A. González, M. Hannam, S. Husa, U. Sperhake, and W. Tichy, Phys. Rev. D **77**, 024027 (2008).
[56] B. Brügmann, W. Tichy, and N. Jansen, Phys. Rev. Lett. **92**, 211101 (2004).
[57] M. Thierfelder, S. Bernuzzi, and B. Brügmann, Phys. Rev. D **84**, 044012 (2011).
[58] J. D. Brown, Phys. Rev. D **79**, 104029 (2009).
[59] P. J. Montero and I. Cordero-Carrión, Phys. Rev. D **85**, 124037 (2012).
[60] I. Cordero-Carrión and P. Cerdá-Durán, arXiv:1211.5930.
[61] M. Shibata, Phys. Rev. D **55**, 2002 (1997).
[62] M. Shibata and K. Uryū, Phys. Rev. D **62**, 087501 (2000).
[63] http://trilinos.sandia.gov.
[64] M. A. Heroux, R. A. Bartlett, V. E. Howle, R. J. Hoekstra, J. J. Hu, T. G. Kolda, R. B. Lehoucq, K. R. Long, R. P. Pawlowski, E. T. Phipps, A. G. Salinger, H. K. Thornquist, R. S. Tuminaro, J. M. Willenbring, A. Williams, and K. S. Stanley, ACM Trans. Math. Softw. **31**, 397 (2005).